

MWC 297: a young high-mass star rotating at critical velocity[★]

B. Acke^{1,★★}, T. Verhoelst^{1,7,★★}, M.E. van den Ancker², P. Deroo¹, C. Waelkens¹, O. Chesneau³, E. Tatulli⁴,
M. Benisty⁵, E. Puga¹, L.B.F.M. Waters^{1,6}, A. Verhoeff⁶, and A. de Koter⁶

¹ Instituut voor Sterrenkunde, KULeuven, Celestijnenlaan 200D, B-3001 Leuven, Belgium
e-mail: bram@ster.kuleuven.be

² European Southern Observatory, Karl-Schwarzschild-Str. 2, D-85748 Garching bei München, Germany

³ Observatoire de la Côte d'Azur/CNRS, BP 4229, 06304 Nice Cédex 4, France

⁴ Osservatorio Astrofisico di Arcetri, L.go E. Fermi, 5, 50125 Firenze, Italy

⁵ Laboratoire d'Astrophysique de l'Observatoire de Grenoble, BP 53, F-38041 Grenoble Cédex 9, France

⁶ Sterrenkundig Instituut 'Anton Pannekoek', Kruislaan 403, 1098 SJ Amsterdam, the Netherlands

⁷ University of Manchester, Jodrell Bank Centre for Astrophysics, Manchester, M13 9PL, U.K.

Received –; accepted –

ABSTRACT

Context. MWC 297 is a nearby young massive B[e] star. The central star is attenuated by 8 magnitudes in the optical and has a high projected rotational velocity of 350 km s^{-1} . Despite the wealth of published observations, the nature of this object and its circumstellar environment is not understood very well.

Aims. With the present paper, we intend to shed light on the geometrical structure of the circumstellar matter that is responsible for the near- to mid-infrared flux excess.

Methods. The H-band ($1.6\text{--}2.0 \mu\text{m}$), K-band ($2.0\text{--}2.5 \mu\text{m}$), and N-band ($8\text{--}13 \mu\text{m}$) brightness distribution of MWC 297 was probed with the ESO interferometric spectrographs AMBER and MIDI, mounted on the VLTI in Paranal, Chile. We obtained visibility measurements on 3 AMBER and 12 MIDI baselines, covering a wide range of spatial frequencies. Different models (parametrized circumstellar disks, a dusty halo) were invoked to fit the data, all of which fail to do so in a satisfying way. We approximated the brightness distribution in H, K, and N with a geometric model consisting of three Gaussian disks with different extents and brightness temperatures. This model can account for the entire near- to mid-IR emission of MWC 297.

Results. The circumstellar matter around MWC 297 is resolved on all baselines. The near- and mid-IR emission, including the silicate emission at 10 micron, emanates from a very compact region ($\text{FWHM} < 1.5 \text{ AU}$) around the central star.

Conclusions. We argue that the extinction towards the MWC 297 star+disk system is interstellar and most likely due to remnants of the natal cloud from which MWC 297 was formed. Furthermore, we argue that the circumstellar matter in the MWC 297 system is organized in a circumstellar disk, seen under moderate ($i < 40^\circ$) inclination. The disk displays no inner emission-free gap at the resolution of our interferometric observations. The low inclination of the disk implies that the already high projected rotational velocity of the star corresponds to an actual rotational velocity that exceeds the critical velocity of the star. This result shows that stars can obtain such high rotation rates at birth. We discuss the impact of this result in terms of the formation of high-mass stars and the main-sequence evolution of classical Be stars.

Key words. Techniques: interferometric; circumstellar matter; Stars: pre-main-sequence; Stars: rotation; Stars: emission-line, Be; Stars: individual: MWC 297

1. Introduction

At a distance of 250 pc and with a stellar mass of approximately $10 M_\odot$ (Drew et al. 1997), MWC 297 is one of the closest massive young stars. It is therefore an ideal target for studying the formation process of massive stars. The source has been the subject of many investigations, covering the entire spectral range from X-rays to centimeter wavelengths (Vink et al. 2005; Damiani et al. 2006; Drew et al. 1997; Andriillat & Jaschek 1998; Malbet et al. 2007; Terada et al. 2001; Benedettini et al. 2001; Acke & van den Ancker 2004, 2006; Henning et al. 1998; Manoj et al. 2007; Palla & Prusti

1993; Han et al. 1998; Skinner et al. 1993). The image that emerges from these studies is far from uniform.

Based on an optical spectrum, Drew et al. (1997) have shown convincingly that MWC 297 is a highly attenuated B1.5V star ($A_V \approx 8$). They derive a distance to the source of 250 pc. Furthermore, these authors indicate that the star is a rapid rotator ($v \sin i = 350 \pm 50 \text{ km s}^{-1}$) and suggest that its rotation axis must be almost in the plane of the sky. The MERLIN 5 GHz data, presented in the same article, display a north-south elongation, along $\text{PA}=165^\circ$ E of N. Drew et al. point out that this elongation may reflect the equatorial plane of a disk-like circumstellar structure around MWC 297. Both the high rotational velocity and the elongated radio structure are consistent with the presence of an edge-on accretion disk, which is the byproduct of the stellar formation of MWC 297.

Near-IR interferometric observations, both broad-band (Millan-Gabet et al. 2001; Eisner et al. 2003; Monnier et al. 2006) and spectrally dispersed (Malbet et al. 2007), have shown

Send offprint requests to: B. Acke

[★] Based on observations made with ESO telescopes at the La Silla Paranal Observatory under program IDs 077.D-0071(B-C), 077.D-0095(C-F), 079.C-0012(A-H) and 079.C-0207(A).

^{★★} Postdoctoral Fellows of the Fund for Scientific Research, Flanders.

that the radiation emitted by the hot circumstellar dust is confined to a very small region around the central star (ring diameter of 1.4 AU, Monnier et al. 2006). They suggest that the circumstellar dust around MWC 297 is located in an accretion disk. In a non-accreting disk (i.e. a *passive* disk in the terminology of Dullemond et al. 2001) the temperature and density structure is predominantly determined by the stellar irradiation. Such a disk has a significant inner disk gap, due to dust sublimation close to the star. The source would display a much more extended, hence more resolved, brightness distribution on the sky. In contrast to the conclusion of Drew et al. (1997), Malbet et al. (2007) suggest an almost pole-on orientation of the accretion disk, based on the analysis of one spectro-interferometric AMBER measurement and regular spectroscopy of the H α , H β and Br γ lines. Their best model consists of a geometrically flat, optically thick accretion disk viewed under an inclination of approximately 20°. The hydrogen lines can be reproduced with a stellar-wind model which has a density enhancement close to the disk's surface. This could point to the presence of a disk wind.

Spectropolarimetric observations of the H α emission show no difference in linear polarization with respect to the continuum (i.e. line effect). This suggests a spherical or circle-symmetric emission region (Oudmaijer & Drew 1999), which supports the low inclination found by Malbet et al. (2007).

Recently, Manoj et al. (2007) have presented 1.3 millimeter (mm) interferometric observations of MWC 297. They show that the mm spectral slope of the spectral energy distribution (SED) is indicative of grain growth in the circumstellar environment, or a very compact structure which is optically thick at mm wavelengths. Manoj et al. (2007) also study the CO emission around MWC 297. They find an extended optically thick CO cloud at $v_{\text{LSR}} \approx 10 \text{ km s}^{-1}$ which is resolved out in their interferometric observations. No compact CO emission region, associated to the mm-continuum of the MWC 297 system, is found. The authors interpret the latter as evidence of strong depletion of CO in the disk.

2. Observations

2.1. Interferometry

MWC 297 was observed in the near- and mid-infrared with the interferometric instruments AMBER (Petrov et al. 2007) and MIDI (Leinert et al. 2003). Both instruments are mounted on the VLTI¹. The observations were performed with the 1.8m Auxiliary Telescopes (ATs) in different baseline configurations. In this paper, we use the VLTI nomenclature to refer to the different telescope stations and baseline settings.

AMBER simultaneously combines the light of three telescopes and currently operates in H- and K-band (1.6–2.5 μm). The fringes are spectrally dispersed. Our data were taken in the low spectral resolution mode (R \sim 30, LR–HK mode). The data reduction was performed according to the methods described in Tatulli et al. (2007). Each observation consists of a number of frames, i.e. exposures with short integration times. We have tested different frame-selection algorithms (e.g. the suppression of frames with low photon counts in the photometric channels; the selection of frames with statistically significant piston estimates; the selection of frames with high signal-to-noise visibility estimates), which were applied to both the target and the calibrator star. Typically, 60–100% of the frames were selected. Little difference is seen between the resulting calibrated visibilities, which confirms the excellent quality of the AMBER

data. Furthermore, we have repeated the AMBER observations on the same baselines to check their consistency. The results of both –independent– observations are equal within the error bars. We have averaged both measurements to obtain the final set of AMBER visibility data.

Thanks to the combination of 3 telescopes, AMBER also provides a spectrally dispersed closure phase (CP) measurement. To estimate the uncertainty on the latter, we take the standard deviation of the closure phase measurement of the calibrator, which is expected to have a zero closure phase. The closure phase of MWC 297 is within the error bars equal to zero ($|\text{CP}| < 5^\circ$). Brightness distributions on the sky that display deviations from centro-symmetry should always display a non-zero closure phase, except at specific combinations of positions in the (u,v)-plane where phases happen to sum up to zero. This is also true if the baselines in the triangle are aligned, which is the case for our observations. Hence, the zero AMBER closure phase strongly suggests the circumstellar geometry of MWC 297 is point-symmetric along the position angle of the baselines, at the spatial resolution of our observations.

We have extracted the H- and K-band AMBER spectrum of MWC 297 from the three photometric channels. The flux in each channel is summed over all frames, and calibrated using the total flux in the corresponding channel of the calibrator star. A photospheric model of the calibrator star is applied to convert to flux units. Finally, the absolute flux level of the AMBER spectrum is determined by multiplicative scaling to the mean value of the Infrared Space Observatory Short Wavelength Spectrograph (ISO–SWS) spectrum (Benedettini et al. 2001; Acke & van den Ancker 2004) in the overlap region between both (2.36–2.5 μm). The error on the spectral shape of the spectrum is determined from the rms of the three photometric channels. We note that the aperture of the ISO–SWS instrument at the shortest wavelengths is 14'' \times 20'', much larger than the seeing-limited resolution of a 1.8m telescope. However, ground-based photometric measurements are in agreement with the ISO flux levels. This indicates that the fraction of extended emission on a large scale is negligible, and that the scaling of the AMBER spectrum to the ISO spectrum is allowed.

MIDI is a two-beam combiner which operates in N-band (8–13 μm). The fringes are spectrally dispersed at a resolution of 30 (HIGH-SENS PRISM mode). We have used the MIA+EWS² data reduction packages to obtain calibrated visibilities. The so-called incoherent (based on power-spectrum analysis of the fringes) and coherent (based on the information contained in the spectrally dispersed fringes) data reduction results are consistent with each other, which indicates the good quality of the data set. Furthermore, the coherent analysis provides differential phases. The latter are within the error equal to zero on all MIDI baselines. This suggests that also the N-band emission region, including the silicate feature, does not deviate much from centro-symmetry.

The MIDI spectrum is determined in the following manner: The raw spectrum of the science target is obtained by adding all photometry files. It is flux-calibrated as described by van Boekel (2004) with the corresponding quantity of two calibrators, or two separate measurements of the same calibrator, observed in the same night as MWC 297 and spaced in airmass. Again, model photospheres were applied to compute the theoretical spectrum of the calibrators. The angular extent of the calibrators was used to scale the spectra to the right absolute flux level. This procedure was obviously only possible in nights were more than one

¹ <http://www.eso.org/projects/vlti/>

² <http://www.strw.leidenuniv.nl/~koehler/MIA+EWS-Manual/>

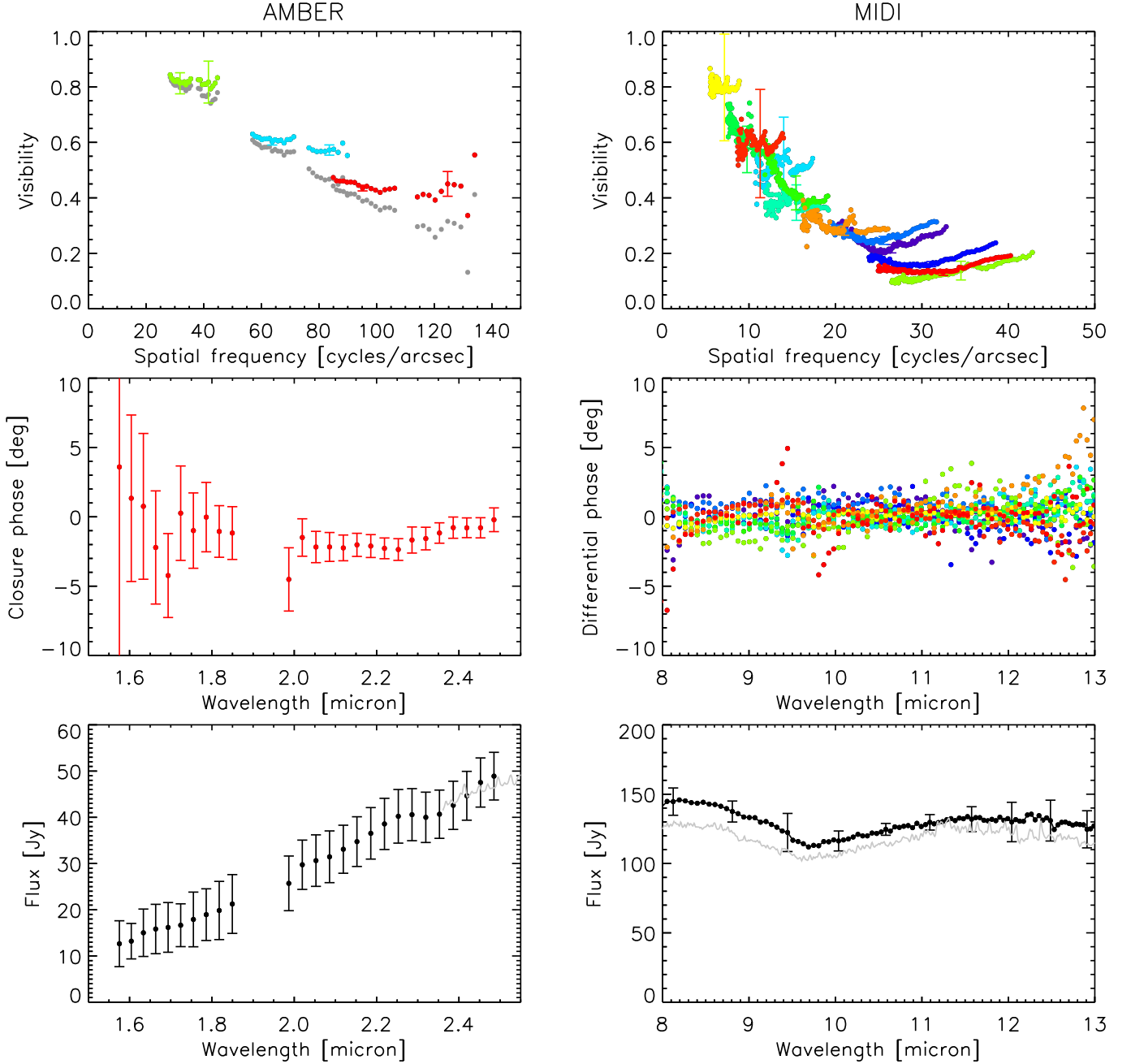


Fig. 1. Interferometric data. *Left, top to bottom:* the calibrated AMBER visibilities, closure phases and spectrum. *Right, top to bottom:* the calibrated MIDI visibilities, differential phases and spectrum. Different colors refer to different baselines. In the top left panel, the AMBER data corrected for the flux contribution of the central star are overplotted in grey (see Sect. 3.1). The grey line in the bottom panels is the ISO spectrum of MWC 297 (Acke & van den Ancker 2004). Representative error bars are overplotted, except for the MIDI differential phases; the average uncertainty on this quantity is 1 degree, consistent with the spread of the data around zero. [This figure is available in color in the electronic version.]

calibrator was observed in the same MIDI setting. We obtain 9 independently calibrated spectra. The final MIDI spectrum is the average of these, with the error being the standard deviation. It is striking that the independently calibrated ISO spectrum and MIDI spectrum of MWC 297 have the same shape and flux level, consistent with the IRAS $12\ \mu\text{m}$ flux, despite the very different aperture size or field-of-view of the respective instruments. This argues in favor of a mid-IR emission region which is spatially

unresolved by a single telescope. The entire N-band emission region is hence sampled by the MIDI interferometer. This conclusion is confirmed by a $11.85\ \mu\text{m}$ VISIR image of MWC 297, in which the source is resolved, but on a much smaller scale than observable with a 1.8m telescope (see Sect. 4.2).

The log of the interferometric observations can be found in Table 1. The calibrator stars are indicated as well. The resulting visibilities, closure phases and spectra are plotted in Fig. 1.

The visibilities are shown as a function of spatial frequency B/λ , with B the projected baseline length and λ the wavelength of the observations. The spatial frequency is a measure for the resolving power obtained with a certain measurement. To guide the reader who is not an interferometry expert: each measurement at a certain baseline consists of a *spectrum* of visibilities and phases, which not only sample a different wavelength, but also a different spatial frequency *and* direction on the sky. Visibility measurements at the same spatial frequency may therefore differ due to a different baseline position angle and/or the spectral dependence of the source's emission on the sky. In the top right panel of Fig. 1, the MIDI visibilities are presented. Here, it can be seen that the 10 micron silicate feature leaves a spectral imprint on the visibilities. We will come back to this in Sect. 3.2.3.

2.2. Additional data

We have expanded our data set with previously published photometric and spectroscopic data. In Fig. 7, the dereddened SED is shown, including the ISO spectrum. The photometric data were taken from Berrilli et al. (1987), Mannings (1994), de Winter et al. (2001), and the 2MASS and IRAS catalogues. The central star is modeled with a Kurucz model for a B1.5V star ($T_{\text{eff}} = 25,400\text{K}$, $\log g = 4.0$). The stellar radius, obtained from the fit of the photosphere model to the UV and optical photometry, is $8 \pm 2 R_{\odot}$. The R- and I-band photometric points were excluded from this fit, since excess flux is present at these wavelengths ($\sim 40\%$ and 20% respectively). The excess in R can be entirely attributed to the extremely strong $H\alpha$ emission in MWC 297. Also the I-band excess is due to hydrogen emission lines. The Paschen lines measured by Andrillat & Jaschek (1998) account for the entire excess. We have applied the interstellar dereddening law of Savage & Mathis (1979), extended to infrared wavelengths with the law described by Steenman & Thé (1989, 1991). We set $R_V = 3.1$ and $E(B-V) = 2.5$, leading to $A_V = 7.75$, consistent with Drew et al. (1997). The AMBER, MIDI and ISO spectra are plotted in Fig. 2. After dereddening, the ISO spectrum displays a weak but significant 10 micron silicate emission feature. The infrared excess luminosity L_{IR} is only 5% of the stellar luminosity L_{\star} .

In Section 4.1, we argue that the extinction of the central star is most likely due to a foreground interstellar molecular cloud, in between the observer and the MWC 297 system. Therefore, the *real* spectrum of the MWC 297 system is the dereddened spectrum. In the following, we use the dereddened AMBER, MIDI and ISO spectra, unless otherwise specified. We stress that the dereddening has no direct consequence for the interferometric measurements, since the latter are only sensitive to the normalized brightness distribution of the source at each wavelength.

Diffraction-limited images of MWC 297 in a broad-band filter centered at $11.9 \mu\text{m}$, and intermediate-width filters centered on 11.3 and $11.9 \mu\text{m}$ were obtained with the VLT Imager and Spectrometer for the mid-Infrared (VISIR, Lagage et al. 2004) during the night of April 13-14, 2007. Subtraction of the thermal emission from the sky, as well as the telescope itself, was achieved by chop-nodding in the North-South direction with a throw of $30''$. The effective integration time was 90 seconds in each filter. Calibrator measurements in the same settings were obtained shortly before the science observation. All observations were obtained when the sources were close to zenith (airmass ~ 1.05). The full-width-at-half-maximum (FWHM) of the calibrators' broad-band image is $0.33 \pm 0.01''$, the FWHM of the MWC 297 image is $0.41''$.

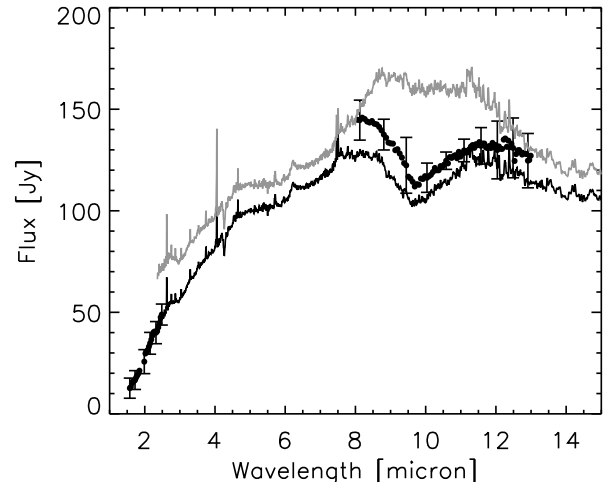


Fig. 2. ISO (black line), AMBER (dots) and MIDI (dots) spectra of MWC 297. The AMBER spectrum was scaled to the ISO spectrum in the overlap region between both spectra. The MIDI spectrum has been calibrated independently and agrees well with the ISO spectrum. In grey, the ISO spectrum is shown, dereddened with the same extinction law as the optical photometry. A mild but significant silicate emission feature is present at 10 micron.

MWC 297 has been observed during a Science Verification run of the Atacama Pathfinder Experiment (APEX³). The APEX-2A heterodyne receiver⁴ mounted on this telescope provided a raster map of the CO (3 – 2) emission line at 345.79 GHz in a $1' \times 1'$ field around the source, with a beam size of $17.5''$. No spatial dependence of the spectrum has been detected in the field, indicating that the detected emission lines are due to a CO structure, significantly larger than the mapped area. This is in agreement with the results of Manoj et al. (2007), who attribute this emission to interstellar clouds. In Fig. 3, the field-averaged spectrum is shown. No features are detected at high red- or blueshift. The latter excludes the presence of a strong CO outflow in MWC 297, on top of the non-detection of CO by Manoj et al. (2007) in the circumstellar disk.

3. Analysis

3.1. Simple geometric modeling

We have fitted simple analytic models to the visibility data. Because the AMBER closure phases and the MIDI differential phases are consistent with zero on all baseline settings, we have only applied point-symmetric and concentric models. The brightness distributions in the H-, K-, and N-bands may be dominated by different components. Therefore, we have first analyzed the data in the near- and mid-IR separately. In the last part of this section, we confront the results and construct a model which fits the interferometric observations and spectra in both wavelength ranges simultaneously.

³ This publication is based on data acquired with the Atacama Pathfinder Experiment (APEX). APEX is a collaboration between the Max-Planck-Institut für Radioastronomie, the ESO, and the Onsala Space Observatory.

⁴ <http://www.apex-telescope.org/heterodyne/het345/>

Table 1. The log of the interferometric observations, sorted according to interferometric instrument and increasing baseline length. The first seven columns refer to the observations of MWC 297, the last four to the calibrator’s properties. As a reference, the wavelength-averaged calibrated visibility $\langle V \rangle_\lambda$ is given. The flux of the calibrator is the 2MASS Ks-band magnitude for AMBER observations and the IRAS 12 μm flux for MIDI. PB = projected baseline length; PA = projected baseline angle.

Night yyyy-mm-dd	UT hh:mm:ss	Instrument	Setting	PB <i>m</i>	PA $^\circ$ E of N	Airmass	$\langle V \rangle_\lambda$	Calibrator	Sp.T.	Diameter <i>mas</i>	Flux <i>mag</i> or <i>Jy</i>
2007-04-14	08:09:13	AMBER	E0-G0	14.2	68.4	1.16	0.78	HD 166460	K2III	1.40	2.58
2007-06-19	07:10:31	AMBER	E0-G0	14.9	73.0	1.20	0.86	HD 166460	K2III	1.40	2.58
2007-04-14	08:09:13	AMBER	G0-H0	28.5	68.4	1.16	0.60	HD 166460	K2III	1.40	2.58
2007-06-19	07:10:31	AMBER	G0-H0	29.9	73.0	1.20	0.59	HD 166460	K2III	1.40	2.58
2007-04-14	08:09:13	AMBER	E0-H0	42.7	68.4	1.16	0.46	HD 166460	K2III	1.40	2.58
2007-06-19	07:10:31	AMBER	E0-H0	44.4	73.0	1.20	0.41	HD 166460	K2III	1.40	2.58
2007-04-12	08:22:50	MIDI	E0-G0	14.3	68.5	1.15	0.79	HD 148478	M1.5I	25.92	3200
2006-04-20	06:02:07	MIDI	D0-G0	20.1	56.3	1.58	0.63	HD 146051	M0.5III	9.83	150
2007-04-17	06:50:30	MIDI	G0-H0	23.4	61.9	1.37	0.60 ^a	HD 82668	K5III	6.99	73
								HD 187642	A7V	3.22	33
2006-04-20	07:57:03	MIDI	D0-G0	28.9	68.8	1.13	0.51	HD 168454	K3III	5.78	62
2006-04-21	09:09:21	MIDI	D0-G0	31.8	72.1	1.07	0.46	HD 167618	M3.5III	11.33	214
2006-04-22	09:59:19	MIDI	D0-G0	31.9	73.1	1.09	0.38	HD 168454	K3III	5.78	62
2007-04-19	08:00:32	MIDI	E0-H0	43.3	68.8	1.14	0.30	HD 187642	A7V	3.22	33
2006-05-23	05:06:38	MIDI	A0-G0	52.6	66.0	1.23	0.27	HD 167618	M3.5III	11.33	214
2006-05-25	05:12:08	MIDI	A0-G0	54.5	67.1	1.19	0.25	HD 146051	M0.5III	9.83	150
2006-05-25	07:20:53	MIDI	A0-G0	64.0	72.7	1.07	0.18	HD 146051	M0.5III	9.83	150
2007-05-10	05:45:56	MIDI	G1-H0	66.8	172.9	1.27	0.14	HD 167618	M3.5III	11.33	214
2007-05-08	06:41:00	MIDI	D0-G1	71.5	129.5	1.14	0.13	HD 167618	M3.5III	11.33	214

^a The calibrators HD 82668 and HD 187642 were observed at high airmass (~ 2), which hampers a reliable calibration. We have averaged the calibrated visibilities. The large errors (Fig. 1) were deduced from the standard deviation.

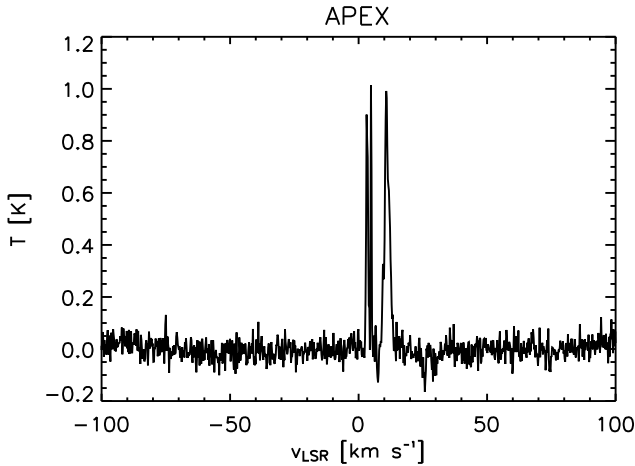


Fig. 3. APEX spectrum of the CO (3 – 2) emission line, averaged over a $1' \times 1'$ field around MWC 297. The three detected features in the v_{LSR} -range between 2 and 13 km s^{-1} are spatially extended and most likely produced in interstellar clouds. No features exceeding the noise level are detected at any other velocity.

3.1.1. Fit to the MIDI data

Most of the MIDI data are obtained on baselines along the VLTI 0-line (i.e. projected baseline angle $\sim 70^\circ$). We are hence predominantly sensitive to the N-band brightness distribution projected onto this direction. The flux contribution of the central star in the N-band is expected to be less than 0.5% and is therefore neglected in the fits described below.

For each observational wavelength, the MIDI visibility curve shows a steady decline with increasing spatial frequency. Strong lobes are absent, although a drop-off may be present at spatial

frequencies around 30 cycles per arcsec. One-component uniform disk (UD), uniform ring (UR) and Gaussian disk (GD) models cannot fit this shape. Two-concentric-component models (UD + point source, GD + point source⁵, two UD, two GD) do better. In general, the GD models do better than the UD models (a factor two in reduced chi-square). In the best-fit ring models, the inner gap is always smaller than 1 mas (0.25 AU at 250 pc). The ring models are thus essentially equal to the uniform-disk models. We have summarized the best-fit parameters of some illustrative models in Table 2. The amount of free parameters in the two-component models was alternated. First, we have fitted the extent of both components, and allowed for a wavelength-dependent linear slope of the flux ratio (model type A in Table 2). The extent of the components was constrained to be the same over the N-band. Hence, this model is fully determined with only 4 parameters. Second, the extent of the components is again wavelength-independent, but now the flux ratio at each wavelength is a free fitting parameter (model type B). The total number of parameters is 2 plus the number of wavelength points. Finally, we have also fitted models in which both the extent and the flux ratio are wavelength-dependent (model type C). Models including point sources have worse χ_{red}^2 values and are therefore excluded from the table. The best model is a 2GD model with all parameters λ -dependent, with a χ_{red}^2 close to 1. The best 2UD model *overfits* the data ($\chi_{\text{red}}^2 = 0.6$).

A number of authors (e.g. Malbet et al. 2007; Manoj et al. 2007) have suggested that MWC 297 is surrounded by an accretion disk. Therefore, we have fitted an alpha-disk (AD) model, in which it is assumed that each annulus around the central star radiates as a blackbody. The temperature at each distance from the star is parametrized with a power law $T(R) \propto R^\alpha$. The six free parameters of this model are the inner and outer radius, the temper-

⁵ Note that the point source in these models does not represent the central star, but an unresolved disk component.

Table 2. Results of some illustrative analytic model fits to the MIDI visibilities. The extent of the model components C1 and C2 is the wavelength-averaged FWHM for GDs and diameter for UD. The wavelength-averaged flux ratio is included as well. #p is the number of fitting parameters in the model, χ_{red}^2 the reduced chi-square value. # λ is the total number of wavelength bins in one MIDI observation. See text for an explanation on the model types.

Model type	Best-fit parameters			#p	χ_{red}^2
	Extent C1 <i>mas</i>	Extent C2 <i>mas</i>	Flux ratio C2/C1		
2 UD _s A	65	23	0.74	4	4.2
2 GD _s A	38	10	0.28	4	2.8
2 UD _s B	65	23	0.79	# λ +2	3.6
2 GD _s B	40	12	0.38	# λ +2	1.9
2 UD _s C	96	32	1.44	3 \times # λ	0.6
2 GD _s C	79	20	1.35	3 \times # λ	1.1

Table 3. Results of alpha-disk (AD) fits to the MIDI visibilities. The alpha disk is determined by the inner and outer disk radius R_{in} and R_{out} , the disk inclination i and position angle PA, and the temperature law $T = T_0 (R/R_{\text{in}})^\alpha$. #p is the number of fitted parameters in the model, χ_{red}^2 the reduced chi-square value of the visibilities.

Model	Best-fit parameters		#p	χ_{red}^2
	T_0	α		
AD	$T_0 = 1510$ K	$\alpha = -0.68$	5	4.9
	$R_{\text{in}} = 4$ mas	$i = 40^\circ$		
	$R_{\text{out}} = 320$ mas ^a	PA = 160°		
Standard accretion disk	$T_0 = 1650$ K	$\alpha = -0.75^a$	4	6.9
	$R_{\text{in}} = 4$ mas	$i = 45^\circ$		
	$R_{\text{out}} = 320$ mas ^a	PA = 150°		

^a Fixed a priori.

ature at the inner radius and the power of the temperature law, the inclination of the disk and the position angle of the major disk axis on the sky. In a standard accretion disk, the temperature drops off with radius proportional to $R^{-0.75}$. An accretion disk can therefore be modeled with an alpha disk in which the power is set to -0.75 . The parameters of the best-fit AD models to the MIDI data are summarized in Table 3. The outer radius of the disk is ill-defined by our data set, i.e. equally good fits can be obtained with any value for this parameter. We have therefore fixed R_{out} to the maximum outer radius determined by Manoj et al. (2007, 80 AU) from mm-observations. The AD models produce a spectrum, which is constrained by the observed MIDI spectrum. Reasonable fits can be obtained, although the simple two-component models presented in Table 2 appear to be much better.

The main conclusion in this section is that simple analytic two-component models do a much better job in reproducing the observed MIDI visibilities than single-component models, a uniform ring or an alpha disk. Two circumstellar structures are present in the MWC 297 system; a smaller structure with a radius of ~ 10 mas (2.5 AU at 250 pc) and a larger structure of ~ 40 mas (10 AU). Note that both components are extremely compact, given the strong radiation of the central B1.5V star. In fact, both structures reside entirely within the 1500K dust sublimation radius of 15 AU for small ($0.1 \mu\text{m}$) amorphous olivine grains.

Table 4. Results of some illustrative analytic model fits to the AMBER visibilities, corrected for the flux contribution of the central star. The nomenclature is the same as in Table 2. See text for details.

Model type	Best-fit parameters			#p	χ_{red}^2
	Extent C1 <i>mas</i>	Extent C2 <i>mas</i>	Flux ratio C2/C1		
UD+P	14.6	–	0.77	2	2.5
UR+P	0.2	7.3	0.44	3	2.5
GD+P	8.3	–	0.46	2	1.6
2 UD _s	23.2	7.3	3.6	3	0.9
2 GD _s	14	4.3	2.8	3	0.7

3.1.2. Fit to the AMBER data

Our observations in the H- and K-band are sensitive to the hottest circumstellar matter present in the MWC 297 system. At these wavelengths, also the central star is a contributor to the total flux. The stellar radius of $8 R_\odot$ corresponds to an angular radius of 0.15 mas. At the spatial resolution of our AMBER observations, the star is therefore completely unresolved and can be treated as a point source.

Supported by the zero closure phase, we assume that the photocenter of the circumstellar emission coincides with the central star. For each wavelength bin, we can then extract the visibility V_{csm} of the circumstellar matter from the measured visibility V_{meas} using

$$V_{\text{meas}} = \frac{F_\star V_\star + F_{\text{csm}} V_{\text{csm}}}{F_\star + F_{\text{csm}}},$$

with $V_\star = 1$, and F_\star and F_{csm} the (uncorrelated) flux of the star and the circumstellar matter respectively. The latter are computed from the AMBER spectrum and the photospheric model of the central star that fits the SED. In H-band, the stellar flux contribution adds up to 20%, in K to 10%. Hereafter, we refer to V_{csm} as the AMBER visibilities, unless otherwise indicated.

Simple analytic models were fitted to the AMBER data. In Table 4 we summarize some illustrative results. All models have wavelength-independent parameters, apart from the initial correction of the visibilities for the star-to-disk flux ratio. Increasing the complexity of the models, e.g. by allowing a flux ratio of the components that varies with wavelength, only decreases the quality of the fit in terms of reduced chi-square due to the small number of AMBER data points. We note that the best-fit UR models prefer a disk which has no inner gap ($R_{\text{in}} < 0.2$ mas $\approx R_\star$). As a result of this, the UR and UD fits are basically the same, with comparable χ_{red}^2 values. It is remarkable that two-component models, with a fixed extent and flux ratio over the H- and K-band, explain the AMBER data very well within the observational errors. A fit with an alpha-disk model to the AMBER data alone is not possible, given the small number of AMBER points, and the fact that all AMBER baselines are aligned: the inclination and position angle of the disk are not constrained, the other parameters vary over a broad range in parameter space. The parameter α , however, can be restricted based on the slope of the visibility curve with wavelength. It appears to lie preferentially in the range between -0.6 and -0.5 , instead of around the standard value for an accretion disk (-0.75).

3.2. Combining AMBER and MIDI

3.2.1. Disk models

The major advantage of the combination of near-IR AMBER and mid-IR MIDI data is the sensitivity to the temperature gradient of the circumstellar matter. Analytic alpha-disk models can therefore be subjected to a constraining test. The models are not only constrained by the visibilities, but also by the spectra in H, K and N. The best-fit standard accretion disk (α fixed to -0.75) has a reduced chi-square of more than 60 and can therefore be ruled out. Leaving the power of the temperature law free, the best fit is obtained with $R_{\text{in}} = 0.42 \pm 0.06 \text{ AU} = 1.7 \pm 0.2 \text{ mas}$, $R_{\text{out}} = 20 \pm 20 \text{ AU} = 80 \pm 80 \text{ mas}$, a temperature at R_{in} of $1600 \pm 250 \text{ K}$ and a power $\alpha = -0.55 \pm 0.03$. The inclination and position angle of the best-fit alpha disk are $i = 20 \pm 20^\circ$ and $\text{PA} = 180 \pm 50^\circ$ respectively. The latter, as well as the outer radius, are ill-defined by the data set. The reduced chi-square of this model is 8.8. The uncertainties on the best fit parameters are derived from fits to virtual data sets, Monte-Carlo simulated around the original data.

Alpha-disk models fail to reproduce the observations, because the presence of an inner gap is needed in the models to keep the temperatures in the inner disk physical (i.e. not exceeding a few 10,000K). The visibilities show however that no gap in the brightness distribution is present at the resolution of our observations. No secondary lobes are observed in the visibility curves, which is e.g. witnessed by the tendency of the uniform ring model fits to have an inner radius close to the stellar surface. Also passive disk models with an inner disk gap (Dullemond 2002, and subsequent papers), in which the central star is the only heating source of the circumstellar matter, can a priori not explain the observations. If a hypothetical passive disk around MWC 297 is seen under a moderate inclination ($0^\circ < i < 70^\circ$), the inner rim at dust sublimation temperature would dominate the near- to mid-IR brightness distribution. Given the large sublimation radius, a detectable gap would show up. If the system is seen edge-on, its appearance on the sky changes. Although present, a physical gap in the disk would not be detected in the visibilities.

3.2.2. A dusty outflow or halo?

It is suggested that the spectral characteristics of young stellar objects can sometimes be explained without the need for a disk-like geometry but instead assuming a spherical distribution of the dust (e.g. Vinković et al. 2006). Given the unclear origin of the circumstellar material around MWC 297, we deem it necessary to test this hypothesis. To this end, we used the radiative transfer code MoDust (Bouwman et al. 2000; Bouwman 2001) with optical constants from the Jena database⁶.

A dusty outflow

Mass loss through a dusty wind such as those found around evolved stars is an a priori improbable source of the IR excess, as the observed features are crystalline rather than amorphous, with a large continuum contribution suggesting the presence of at least micron-sized grains. Our attempts to model SED and visibilities simultaneously with an outflow model failed in all possible approaches, regardless of the dust species and grain characteristics used: (1) An outflow model matching the SED

characteristics⁷ can be found, with an inner dust radius compatible with its condensation temperature ($R_{\text{in}} = 90 R_\star = 3.5 \text{ AU}$, $T_{\text{in}} = 1500 \text{ K}$), but the derived visibilities are orders of magnitude too small at all wavelengths. (2) Focussing instead on the observed spatial dimensions of the circumstellar structure, it is possible to reproduce the visibilities in the mid-IR in 2 ways: either with a small inner dust radius or starting from the SED-matching model and reducing the outflow to a thin shell at the inner radius. In the first case, the dust which is unshielded from the stellar radiation reaches unrealistic temperatures of 3000 K and, moreover, this hot dust generates such a strong near-IR excess that the AMBER visibilities can not be reproduced. This is the case even when using only mm-sized or oxide grains which resist heating much more than smaller and/or silicate grains. In the second case, the SED is no longer matched, and the dust which is at condensation temperature is still too bright and/or resolved in the near-IR. (3) No way was found to reproduce the AMBER visibilities, even without the constraint of the SED and MIDI visibilities, with anything remotely resembling a dusty outflow.

Other density distributions

We attempted fits with other density distributions as well, using power laws ($\rho(R) = \rho_0 R^\beta$ with ρ the dust density, R the distance from the central star and β the free parameter determining the density gradient) with β ranging from -3 to $+3$. Again, the inner and outer radius were varied but all to no avail: requiring radiative equilibrium for the dust makes it impossible to have it at a temperature of only 500 K (the brightness temperature of the larger component, and the temperature preferred for that component by the analytical models presented in Sect. 3.2.3) so close to the central star without some form of effective shielding. All fitted models have reduced chi-square values over 100.

We conclude from these attempts that a dusty halo, be it an outflow or some other density distribution, can explain none of the components observed with AMBER and MIDI, in spite of good spectral agreement.

3.2.3. Approximating the brightness distribution

No tested physical model (accretion disk, halo, passive disk) is able to explain the observations. Therefore, we aim at approximating the near- to mid-IR brightness distribution of the source using a combination of analytic models. This approach focusses on the fitting of all interferometric data as a whole and, as a by-product, delivers an *image* of the source close to its real appearance on the sky. One should however keep in mind that the analytic components used in the fits do not necessarily have physical meaning. They are merely building blocks for our image. We will come back to this in Sect. 4.

Two component models fit the AMBER and MIDI data well within the errors. The AMBER visibilities, corrected for the contribution of the unresolved central star of the system, are flux-dominated by a small component. In the MIDI data, on the other hand, the most extended component is dominant. The extent of the largest component in the AMBER fits, and the smallest component in the MIDI fits, appears to be of the same order. Furthermore, the closure and differential phases, in HK- and N-band respectively, suggest a point-symmetric source geometry. Inspired by the AMBER and MIDI fits, we have built a concen-

⁷ Due to its large inner radius, this model hardly obscures the photosphere, showing that a low circumstellar A_V alone does not necessarily require a disk-like dust distribution.

⁶ <http://www.astro.uni-jena.de/Laboratory/Database/databases.html>

Table 5. The parameters of the best-fit three-GD model. *Top:* Fit to all interferometric data simultaneously. *Middle:* Fit to subset only. *Bottom:* Inclination and position angle (PA) of the disk’s major axis, based on the visibility measurements obtained on the two baselines with different baseline position angles. The reduced chi-square χ_{red}^2 for each fit is given. See text for details.

3GD fit to all			
FWHM	A		$4.3 \pm 0.2 \text{ mas}$
FWHM	B		$12.3 \pm 0.5 \text{ mas}$
FWHM	C		$41.6 \pm 0.7 \text{ mas}$
FR	A/B	slope	$-1.0 \pm 0.4 \mu\text{m}^{-1}$
		at $2 \mu\text{m}$	2.6 ± 0.4
FL	A	at $10 \mu\text{m}$	$2 \pm 2 \text{ Jy}$
FL	B	at $10 \mu\text{m}$	$45 \pm 2 \text{ Jy}$
χ_{red}^2	4.5		
3GD fit to subset			
FWHM	A		$4.2 \pm 0.3 \text{ mas}$
FWHM	B		$12 \pm 1 \text{ mas}$
FWHM	C		$40.8 \pm 0.7 \text{ mas}$
FR	A/B	slope	$-0.9 \pm 0.4 \mu\text{m}^{-1}$
		at $2 \mu\text{m}$	2.4 ± 0.6
FL	A	at $10 \mu\text{m}$	$8 \pm 5 \text{ Jy}$
FL	B	at $10 \mu\text{m}$	$36 \pm 5 \text{ Jy}$
χ_{red}^2	4.1		
i	$40 \pm 10^\circ$		
PA	$120 \pm 50^\circ$		
χ_{red}^2	3.8		

tric three-component model, consisting of three Gaussian disks (3GD), to fit all visibilities simultaneously. We assume that two of these components are hot enough to radiate in the near-IR, and that the third one represents the cooler material, which is responsible for the 10 micron silicate feature and does not contribute to the AMBER flux. Since the brightness temperatures of the two HK-band components is high (as expected from the AMBER fits), the N-band flux contribution of the two hot components in the 3GD model is represented by the Rayleigh-Jeans tail of a blackbody (i.e. $F_\nu \propto \lambda^{-2}$). This approximation is made to suppress the number of model parameters. In summary, the model has 7 free parameters. The FWHMs of the GDs constitute three of those. Over the AMBER wavelength range (1.6–2.5 μm), we allow for a linear slope of the flux ratio of the two hottest components, implying two additional model parameters. The last two parameters control the absolute flux levels of the blackbody tails of the two hottest components at 10 micron. The flux contribution of the coolest component is then fixed to the N-band spectrum minus these blackbody contributions. At this stage, we do not allow for asymmetry due to inclination. This will be discussed later in this Section.

We fit this model to all visibility data simultaneously. The best-fit parameters and errors are summarized in the upper part of Table 5. The three GD components were labeled A, B and C from small (hot) to large (cold). The parameters are the FWHM of each component, the linear flux ratio (FR) of component A and B in the near-IR, and the absolute flux levels (FL) of components A and B at $10 \mu\text{m}$. The uncertainties on the best fit parameters are derived from fits to one hundred Monte-Carlo simulated data sets, around the original data.

In our data set, two baselines have significantly different position angles than the rest (PA= 170° and 130° versus PA $\approx 70^\circ$ respectively). If present, strong asymmetries in the brightness distribution should be observable at these baselines. Therefore, we have repeated the fit on a smaller data set (hereafter called

the *subset* of data), limited to the data obtained at PA $\approx 70^\circ$. Also these best-fit parameters are included in the middle part of Table 5. We note that the reduced chi-square is noticeably better ($\chi_{\text{red}}^2 = 4.1$ versus 4.5, respectively), although only 85% of the data was used, and the number of free model parameters remained the same. The extent of the three Gaussian disk components are comparable in the two fits, and are 4, 12 and 41 mas respectively. This corresponds to 1, 3 and 10 AU at a distance of 250 pc.

The blackbody brightness (BB) temperatures of the components are deduced from their relative flux contributions to the AMBER+MIDI spectrum. The errors are determined from the rather large errors on the absolute flux level on the spectra, and the uncertainties on the model parameters. The smallest component has a BB temperature of $1700 \pm 200 \text{ K}$, the middle component $930 \pm 80 \text{ K}$. As a consequence of our modeling approach, the spectrum of the largest component contains the 10 micron silicate emission feature, as well as part of the underlying continuum. We have determined the temperature of this component, assuming that its flux is exclusively produced by $0.1 \mu\text{m}$ olivine grains. The best fit was obtained with a temperature of $520 \pm 20 \text{ K}$ and a column density larger than 0.02 g cm^{-2} . The latter value, in combination with the spatial extent of the component, corresponds to a mass in small olivine grains of at least $2 \times 10^{-7} M_\odot$.

To get a handle on the possible elongation of the source’s brightness distribution – e.g. due to inclination – we have taken the 3GD model that fits the subset of data, and applied it to the visibility data obtained on the two baselines with different position angles. We insert one additional fitting parameter, a multiplicative factor that can change the extent of the three components simultaneously depending on baseline position angle. All relative quantities (FWHM ratios, flux ratios) were fixed to the best-fit parameters, while the absolute scaling of the extent of the model was fitted. This method yields a factor at all position angles, which is nominally equal to 1 for the subset of data at PA 70° , and 1.16 ± 0.01 and 1.23 ± 0.03 for the data along PA 170° and 130° . Assuming that the circumstellar structure around MWC 297 is a geometrically flat disk – supported by the low L_{IR} / L_\star ratio of 5% – these numbers can be translated into an inclination and position angle of the major disk axis on the sky of $40 \pm 10^\circ$ and $120 \pm 50^\circ$ respectively. The extent of the components along the disk major axis is 1.3 ± 0.1 times larger than along PA= 70° . The reduced chi-square of the *rescaled* model visibilities, compensated for the additional model parameter, is 3.8 (bottom part Table 5). Although a large inclination is excludable, we caution against overinterpretation of the inclination and disk position angle estimates. The two baselines with different PAs are also the longest baselines, and hence sample a slightly different spatial-frequency domain than the subset. A perfectly spherically symmetric model may therefore fit the data just as well (as was e.g. shown with the MIDI fits). To straighten out the issue and determine the exact inclination, more visibility measurements at comparable spatial frequencies, but different baseline angles, are required.

We consider our fit to the subset of data as our most reliable fit, since no issues related to the position angle are present. The model fit to the visibility data is shown in Fig. 4. In Fig. 5, a radial cut of the intensity distribution of the model at different wavelengths is shown. Note that, although the FWHM of the largest GD component is 40 mas (10 AU), the FWHM of the *total* image is less than 6 mas (1.5 AU) at all wavelengths. The extent of our approximated image of MWC 297 is in perfect agreement with the VISIR image at $11.85 \mu\text{m}$. We have convolved the model image with a Gaussian curve of FWHM $0.33 \pm 0.01''$,

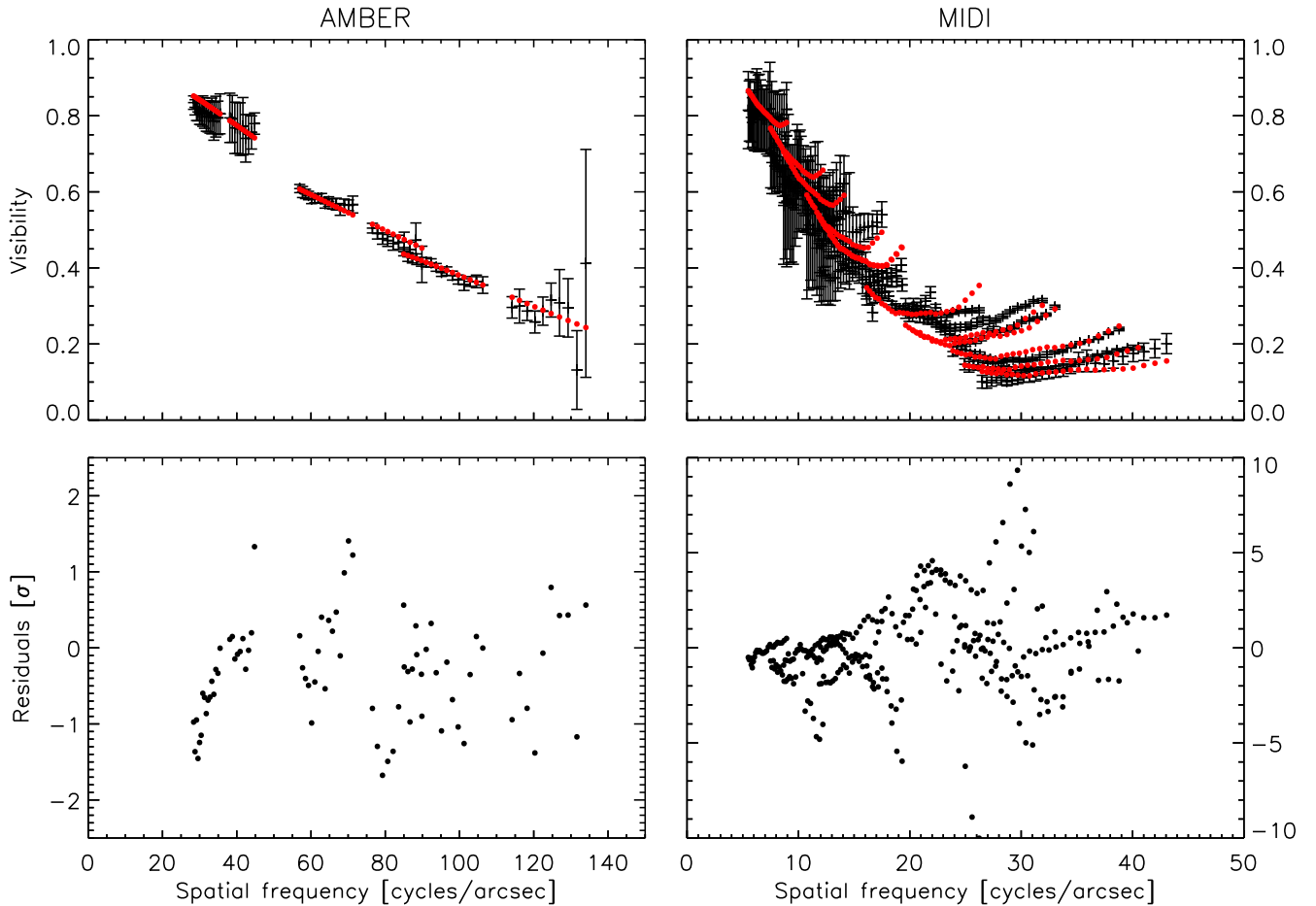


Fig. 4. *Top panels:* Best model fit to the visibility data. The AMBER data are corrected for the stellar flux contribution. The two longest MIDI baselines have different baseline position angles. The model fit to the visibilities related to the latter is the best-fit model which includes the effect of the disk’s inclination, as described in the text. *Bottom panels:* Residual difference between observed and modeled visibilities, expressed in terms of the error σ on the individual measurements. [This figure is available in color in the electronic version.]

to mimic the point spread function estimated from the two calibrator measurements. The resulting image has a FWHM of $0.39 \pm 0.01''$, in perfect agreement with the measured $0.41''$.

We have compared the H-band AMBER and model visibilities to the broad-band visibilities obtained by Monnier et al. (2006) with IOTA. In Fig. 6, their H-band visibilities are shown together with the AMBER visibilities at $1.65 \mu\text{m}$ and the broad-band visibilities of our best-fit model. The IOTA measurements are in relatively good agreement with our data given the large error bars, although they appear to be systematically higher. It is not clear to us why this discrepancy is present. The IOTA H-band data were obtained at different baseline position angles. The smooth decline of the visibilities with spatial frequency, independent of position angle, shows that the circumstellar emission region does not display strong asymmetry. In case of a flat disk, this corresponds to a moderate inclination of *at most* 40° , consistent with our upper limit.

3.3. Consistency with the SED

The brightness temperatures derived for the three components in our best-fit model, are consistent with the near- to mid-IR

SED. The model emission accounts for the total near- to mid-IR flux. In Fig. 7, the contribution of the components to the total flux is shown. The spectrum of the largest component is a single-temperature Gaussian disk consisting of olivines with a column density of 0.02 g cm^{-2} . At sub-mm/mm wavelengths, only the coolest component contributes significantly. The photometric points at these wavelengths are clearly higher than the predicted model flux. This points to the presence of an additional cold dust component, which does not contribute flux at near- to mid-IR wavelengths. Following Manoj et al. (2007), 200 mJy of the 1.3 mm flux can be attributed to dust emission, while the rest is free-free emission from an ionized wind. After subtraction of the contribution of the three warm near-/mid-IR components, 155 mJy remains. The combination of the 1.3 mm flux and the fact that the cold dust does not contribute to the mid-IR flux, places an upper limit of 200K on the brightness temperature of this material, and a lower limit of 160 mas to its extent. The limits set by spatially resolved mm observations ($< 230 \text{ mas}$, Mannings 1994; Manoj et al. 2007), constrain the brightness temperature to more than 100K. The brightness temperature of the cold dust is therefore restricted to the interval between 100 and 200K.

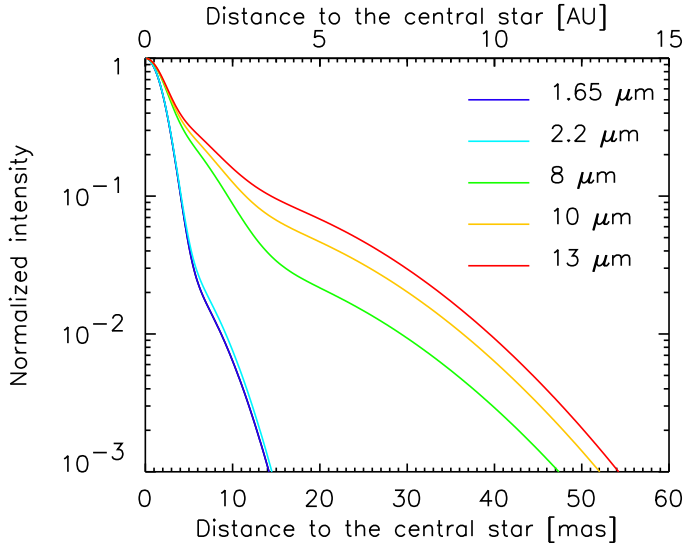


Fig. 5. Radial cut through the normalized intensity distribution of the best-fit model. Different curves refer to cuts at different wavelengths: 1.65, 2.2, 8, 10 and 13 μm . The extent of the model increases with increasing wavelengths. The flux contribution of the central star is excluded from the plot for clarity. [This figure is available in color in the electronic version.]

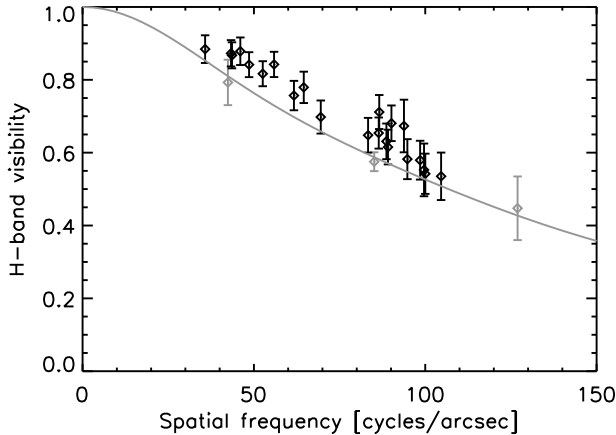


Fig. 6. IOTA broad-H-band data published by Monnier et al. (2006). For comparison, the (narrow-band) AMBER visibilities at 1.65 μm are overplotted in grey, as well as our best-fit model converted to broad-band visibilities (solid line).

Spitzer IRAC images of MWC 297 show very complex cloud structure on arcminute scales (Fig. 8). Its extent and structure coincides with that of the 50–100 μm brightness distribution measured by di Francesco et al. (1994). This cold material is likely responsible for the additional far-IR ($>25 \mu\text{m}$) flux excess, evident in e.g. the IRAS 25, 60 and 100 micron points. Also the ISO–SWS and ISO–LWS (Long Wavelength Spectrograph) spectra, which are obtained with increasing aperture size towards longer wavelengths (Benedettini et al. 2001), suffer from this large-scale emission. It is possible that the mm observations are partially affected by this emission as well, although most of it would be resolved out. At near- and mid-IR wavelengths, the flux contribution of the clouds is negligible: at 8 micron, the total flux adds up to 130 Jy, spread out over roughly 10 square arcminutes. Assuming a homogeneous emission region, the flux

inside the ISO $14'' \times 20''$ aperture would be of the order of 1 Jy ($<1\%$).

4. Discussion

4.1. The extinction towards the MWC 297 system

The flux of the central star in the MWC 297 system is attenuated with 8 magnitudes in V. Drew et al. (1997) suggest that the real extinction could be even stronger, if the observed stellar flux is scattered, rather than direct light. However, this seems unlikely; The application of an interstellar extinction law (Savage & Mathis 1979; Steenman & Thé 1989, 1991, with $A_V = 7.75$ and $R_V = 3.1$), makes that the dereddened photometry agrees with the expected fluxes of a B1.5V star at 250 pc from UV to the optical. In the case of scattering, the observed photometry would have been bluer. Application of an interstellar extinction law would in this case be inappropriate and would yield results inconsistent with a B1.5V model.

A priori, it is unclear whether the attenuation of the central star is due to circumstellar matter, physically linked to the central star, or interstellar dust. However, in the case of MWC 297, the extinction is most likely interstellar. An extended CO cloud is detected in the direction of the target (Manoj et al. 2007). The extent of this cloud is at least $1' \times 1'$, much larger than the extent of the near- and mid-IR emission region of MWC 297. The ISO spectrum of MWC 297 shows H_2O and CO_2 ice absorption bands, indicative of a cold environment. It is improbable that these ices are abundant in a small ($R < 80 \text{ AU}$) and hence warm environment close to a B1.5V star. Furthermore, attenuation of the central star can be described with an interstellar extinction law, where small ($0.1 \mu\text{m}$) grains are the main source of opacity. The presence of small dust grains, CO_2 and H_2O ice, and the large-scale CO emission are naturally explained by an interstellar molecular cloud in between the observer and the MWC 297 system. Moreover, the proximity (0.1 pc at 250 pc) of the large-scale cloud structure present in the Spitzer images –which is also evident from the extended 50–100 μm emission found by di Francesco et al. (1994)– strongly suggests that the latter is remnant material from the natal cloud from which MWC 297 and the nearby lower-mass young stars (Vink et al. 2005; Damiani et al. 2006) were formed. It is probable that the interstellar cloud in the line-of-sight is part of this large structure surrounding the MWC 297 stellar group.

The main consequence of this conclusion for the present paper, is the fact that the entire MWC 297 system (i.e. the central star + the circumstellar matter responsible for the near- to mid-IR flux) is *screened* by this cloud. This is not important for the interpretation of the interferometric data, because the latter are only sensitive to the *normalized* brightness distribution on the sky. Relative quantities (e.g. flux ratios between two components in the interferometric models) can however be transformed into absolute quantities (e.g. brightness temperatures), only if the *un-obscured* spectrum of the system is known. We have dereddened the AMBER, MIDI and ISO spectra of MWC 297 for that purpose, with the same extinction law extending from UV to mid-IR.

4.2. The near- and mid-IR geometry of MWC 297

Our investigation of the near- and mid-IR brightness structure of the MWC 297 system yields the following results:

- MWC 297 is an extremely compact source. The bulk of the near- to mid-IR emission emanates from a region remark-

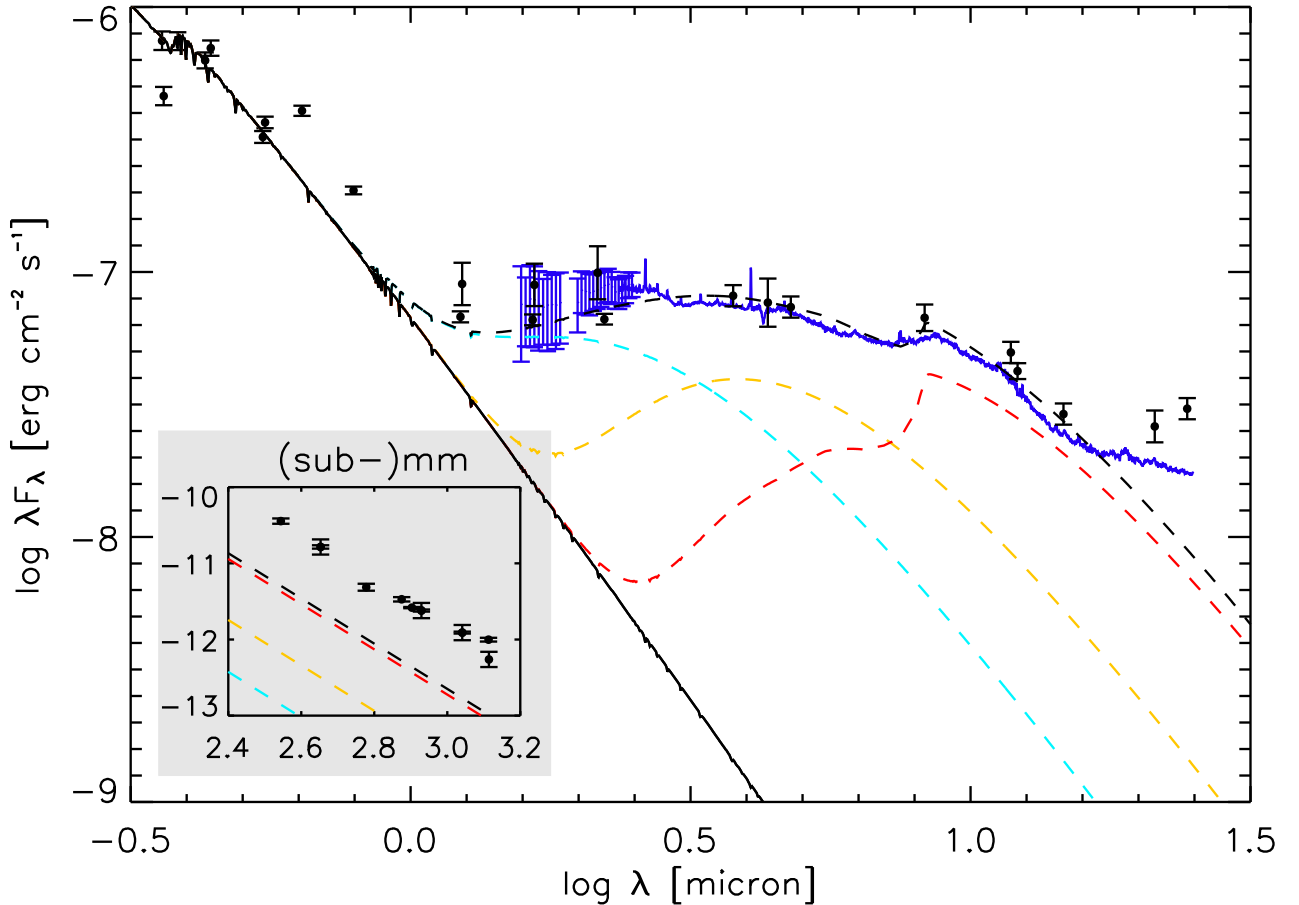


Fig. 7. Dereddened SED of MWC 297. Black dots with error bars are photometric measurements. The full black line is a Kurucz model of a B1.5V star ($T_{\text{eff}}=25400\text{K}$, $\log g=4.0$), the full blue line is the dereddened ISO spectrum. The blue error bars represent the dereddened AMBER spectrum. The flux contribution of the three Gaussian-disk components in the model are shown as dashed lines, adding up to the black dashed line. *Inset:* At sub-mm/mm wavelengths, the model underestimates the observed fluxes, indicating the presence of an additional, cold component in the circumstellar environment of MWC 297. [This figure is available in color in the electronic version.]

ably close to the central B1.5V star. The extent of the system in the H-, K- and N-bands (image FWHM ~ 1.5 AU) is well within the maximal outer radius of the system determined from mm observations ($< 60\text{--}80$ AU, Mannings 1994; Manoj et al. 2007).

- The closure and differential phases obtained with respectively AMBER and MIDI are equal to zero within the errors. There is no evidence of strong deviations from centrosymmetry along a position angle of 70° E of N at the spatial resolution of our observations, neither in the continuum nor the silicate feature.
- There is no significant IR-emission-free gap between the circumstellar matter and the stellar surface at the resolution of our observations.
- Tentative evidence is found for a moderate elongation of the brightness distribution, or a moderate inclination of the circumstellar disk ($i < 40^\circ$). A high inclination is excludable.
- Parametrized accretion disk models cannot explain the data. This either suggests that the circumstellar matter around MWC 297 does not reside in an accretion disk, or that simple models are not appropriate to explain the characteristics at the small angular scales observed.

- A spherically symmetric dusty outflow or halo cannot account for the interferometric and photometric observations either.

We have used geometrical models to approximate the circumstellar brightness distribution of MWC 297, with as few free parameters and analytic components as necessary. Three circumstellar components suffice. However, it is unclear what the physical meaning of these components is. Although it might be that they are independent physical structures, it is more likely that the three Gaussian disks sample the temperature gradient of a smooth density distribution. Our analysis has shown that a power-law approximation of the temperature is inappropriate for the circumstellar matter around MWC 297. Furthermore, the strong radial drop-off of the temperature seems to suggest that the circumstellar matter is optically thick in the radial direction. The halo modeling has shown that an optically thin or moderately thick circumstellar medium produces a much shallower temperature gradient: at the location of the largest geometrical component, the temperature would be much higher than observed. The most likely geometry of the circumstellar matter is therefore a flattened disk, which is viewed under a moder-

ate inclination. However, this disk is significantly different from a typical lower-mass Herbig Ae or T Tauri accretion disk: it is compact and geometrically rather flat (as supported by the low IR excess luminosity).

4.3. On the nature of the circumstellar matter

The circumstellar structure in the MWC 297 system is remarkable in many respects. We highlight some literature results and discuss these in the framework of the present paper.

- The central star rotates with a projected velocity $v \sin i = 350 \pm 50 \text{ km s}^{-1}$ (Drew et al. 1997). Critical rotation occurs when v_{rot} attains $\sqrt{2GM_*/(3R_*)} = 450 \pm 70 \text{ km s}^{-1}$, or equivalently when $i < 55 \pm 15^\circ$. The interferometric measurements suggest a moderate inclination $i < 40 \pm 10^\circ$, and hence that the star is indeed rotating at or close to critical velocity.
- Extremely strong hydrogen emission lines from optical to mid-IR wavelengths are observed. The spectral line profiles are rather narrow ($H\alpha$ FWHM $\sim 200 \text{ km s}^{-1}$) compared to e.g. the half-maximum widths observed in other Herbig Be stars. The extinction of the hydrogen lines is consistent with an A_V of 8 (Drew et al. 1997), which suggests that the hydrogen emission region is attenuated by the same material as the central star.
- The forbidden [O I] emission lines at 6300 and 6363 Å are extremely strong, but also extremely narrow (FWHM $\sim 22 \text{ km s}^{-1}$, Acke et al. 2005). The lines are thermally excited, as proven by the detection of the [O I] 5577 Å line (Andrillat & Jaschek 1998); The line ratio of the 6300 and 5577 Å lines is 5 ± 1 , combining the equivalent width measurements of Andrillat & Jaschek (1998) and Acke et al. (2005). Typical Herbig Be sources (e.g. Z CMa, CD-42°11721, PV Cep, V645 Cyg; Acke et al. 2005) display strong [O I] lines with extended blue wings, up to several hundreds of km s^{-1} . The latter is a strong indication for the presence of a bipolar outflow. If the [O I] emission in MWC 297 also emanates from an outflow, the outflow axis should lie in the plane of the sky (Acke et al. 2005), to match the limited velocity dispersion of the observed spectral lines. Given the small disk inclination, however, it is most probable that the [O I] emission emanates from the disk itself.
- Manoj et al. (2007) find a shallow sub-mm slope of the SED, indicative for the presence of large grains, or an emission region which is optically thick at these wavelengths. The first would indicate grain growth, the former is consistent with a very compact and dense circumstellar disk.
- In the 3–micron range, the spectra of MWC 297 display diamond emission (Terada et al. 2001; Acke & van den Ancker 2006). Diamonds form under conditions of severe temperature and pressure, both of which appear to be present in the circumstellar environment of MWC 297.
- H₂O maser emission has been found by Han et al. (1998) at a v_{LSR} of -75.6 km s^{-1} . The emission is blueshifted by $\sim 85 \text{ km s}^{-1}$ compared to the radial velocity of the central star ($v_{\text{LSR}} = 10 \pm 2 \text{ km s}^{-1}$, based on the peak position of optical emission lines). Palla & Prusti (1993) suggest that in Herbig Be stars the origin of this emission lies in a collimated (bipolar) outflow. The detection of water emission seems to suggest that also MWC 297 drives a molecular outflow, despite the absence of a detected CO outflow, even at high blueshifts (see Fig. 3). Given the strong blueshift, the

outflow axis of the H₂O must be approximately aligned with the line of sight. The receding (redshifted) emission would then be obscured by the circumstellar disk. This is consistent with a small disk inclination.

MWC 297 is a high-mass young star, accompanied by lower-mass newborn stars and remnants of its natal cloud. The central B1.5V star is a critical rotator. It is surrounded by a dense gaseous and dust-rich disk, which reaches in close to the stellar surface and produces the prominent gaseous emission lines in the optical-to-IR spectrum. The star+disk are viewed under a moderate inclination angle.

5. MWC 297: a critical rotator and Be star progenitor

Stellar rotation has, in recent years, been realised to be a fundamental property that can determine the evolution and ultimate fate of high-mass stars (Meynet & Maeder 2000; Maeder & Meynet 2000). Rapid rotation impacts on stellar life times and alters the chemical evolution of the star. Knowing stellar rotation as a function of mass and age is thus essential to understanding high-mass star evolution. In our galaxy, some twenty per cent of all high-mass stars, the classical Be stars, show rapid rotation and associated mass loss. Our identification of MWC 297 as a critical rotator proves that high-mass stars can achieve such high rotation rates at birth. In this section, we discuss the consequences of this discovery. Furthermore, we argue that MWC 297 is an evolutionary progenitor of a classical Be star.

Observations have provided increasing evidence that also high-mass stars form due to mass gain via an accretion disk (Vink et al. 2002), as do solar-mass stars. For the latter, the rotational velocity at birth is thought to be determined by the interaction of the star and its accretion disk (Shu et al. 1994). Magnetic fields lock the stellar surface rotation rate on the orbital rate close to the inner edge of the disk. A high accretion rate, as well as a low magnetic field strength, shifts the distance at which stellar and disk rotation are locked to smaller radius, implicating a higher stellar rotation rate. Therefore, theory predicts that stars with a small inner disk radius have a high surface rotation rate at birth.

The evolution of the equatorial rotation speed of high-mass stars is governed by the combined effects of surface mass loss and the internal redistribution of angular momentum. The first removes angular momentum and is believed to be important for very massive ($M > 25 M_\odot$) stars; its influence for lower-mass stars is unclear (Ekström et al. 2008) but can be significant. Angular momentum redistribution inside the star, however, can result in an increase of the ratio between equatorial rotation speed and the critical velocity. Theory predicts that the critical velocity may be attained for stars of 10–20 M_\odot at a considerable age of 10 million years. On the other hand, very little is known about the rotational velocities of high-mass stars at birth, and theory is currently unable to describe the evolution of stars born at the critical speed. It is in this framework that the critical rotation of MWC 297 attains its full significance.

Two observations imply that a dense and opaque gaseous innermost disk, very close to the stellar surface, shields the outer disk in the MWC 297 system. (1) The occurrence of dust so close to the star is remarkable, as direct stellar irradiation would heat it there far above its sublimation temperature. In lower-mass young stars, stellar irradiation makes the innermost disk dust-free and opens up a gap between star and dust disk (Monnier et al. 2005).

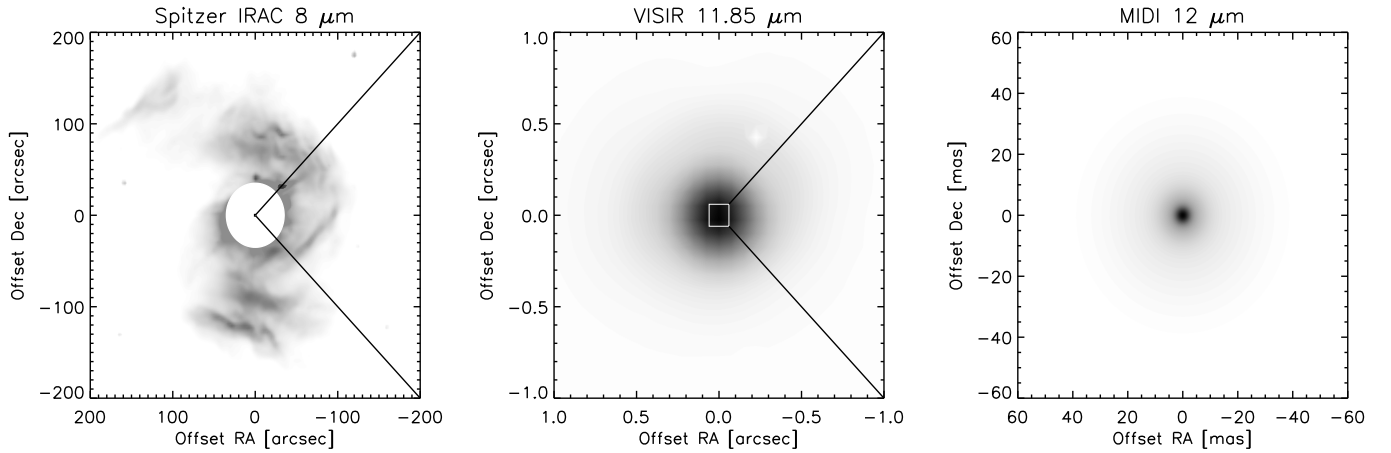


Fig. 8. Traveling to the center of MWC 297. *Left:* Spitzer IRAC image at $8\ \mu\text{m}$. Clearly visible is a complex, large-scale cloud structure. A numerical circular mask covers the saturated part of the image. *Middle:* Zoom-in at the center of the Spitzer image: VISIR image at $11.85\ \mu\text{m}$. The image is seeing-limited, but its FWHM is significantly larger than that of the calibrators. *Right:* Zoom-in at the center of the VISIR image: our best-fit interferometric image at $12\ \mu\text{m}$. The greyscale in the three images is linear.

No such gap is observed in the disk of MWC 297. (2) Given the strength of the optical emission lines but their small radial-velocity dispersion, these lines must mainly originate in the disk, which is at low inclination. A large amount of neutral oxygen and hydrogen atoms are thus present close to the star, which confirms that the ionising stellar photons are absorbed efficiently close to the star.

The fact that this remarkably compact disk encompasses a critically rotating star suggests a causal link. This link could be the formation scenario discussed above. In that case, MWC 297 would either have a weak magnetic field, have experienced high-rate mass accretion, or a combination of both. It would mean that a scenario initially developed for low-mass stars, also applies for their high-mass counterparts. Accretion may still be ongoing in this case. The current observations, however, do not allow for a definite judgement on whether the matter in the innermost disk is moving inward or outward. It cannot be excluded that accretion has ceased, and that the critical rotation of the star currently induces mass loss to the disk through an equatorial outflow. Both hypotheses are consistent with the absence of an inner gap implied by the near- and mid-infrared observations, and the presence of high-density gas very close to the stellar surface.

The discovery of a young star rotating at critical velocity proves that stars can achieve such high rotation rates at birth. This conclusion naturally raises intriguing questions on the initial distribution of rotational rates in newly formed high-mass stars. At this point, it is difficult to estimate the frequency at which critically spinning stars are produced. A hint that this fraction cannot be too small may be found in the proximity of MWC 297: it is the closest high-mass young star known to date, and as such the prime target for investigation. That this particular star rotates at critical velocity suggests that we were either very fortunate, or that fast rotation at birth is more common than generally assumed.

It is tempting to speculate about the future evolution of MWC 297. The star will most likely evolve into a classical Be star. The latter are high-mass main-sequence stars which exhibit line emission produced in a gaseous equatorial disk: the line profiles of the Balmer lines indicate Keplerian rotation and rather small outflow velocities. Since classical Be stars share the common characteristic of faster-than-average stellar rotation, it is likely that strong equatorial centrifugal forces contribute to the

origin of the disks. However, observed rotation velocities do not reach the critical velocity, hence the need to invoke additional effects, such as pulsations or magnetic streams, to explain disk formation (Porter & Rivinius 2003). In a first phase, MWC 297's disk will evolve from dust-rich to purely gaseous: The high density in the innermost disk will decrease, either due to a decrease of the accretion rate, or a decrease of the stellar equatorial mass loss. The disk will eventually become transparent to stellar photons, which will sublimate the dust grains. The neutral oxygen and hydrogen will become ionised, implying the disappearance of the forbidden lines and significantly reducing the strength of hydrogen emission. MWC 297 will then have all the features of a classical Be star.

Our study demonstrates the power of interferometry to determine the initial rotation rates of massive stars. When such studies can be extended to a statistically significant sample, it will become possible to assess whether MWC 297 is an exceptional object or whether critical rotation is the general rule for newborn massive stars. In the latter case, the much slower rotation of most main-sequence stars would imply that the processes which carry away angular momentum are very efficient in our galaxy. In the former case, MWC 297 would qualify as a candidate for the hypothetical objects in which extreme rotational mixing induces an almost homogeneous internal composition throughout the main-sequence phase, hence causing the star to bypass the red-supergiant phase (Maeder 1987). MWC 297 would then be a possible progenitor of a gamma-ray burster (Woosley & Heger 2006) close to our sun. However, gamma-ray bursters appear to occur preferentially in low-metallicity environments (Wolf & Podsiadlowski 2007), where indeed the mass loss and associated angular-momentum losses are expected to be lower than in our galaxy (MacFadyen & Woosley 1999).

Acknowledgements. The authors want to thank J. Monnier for kindly and quickly providing us with the IOTA H-band visibility data. This publication makes use of data products from the Two Micron All Sky Survey, which is a joint project of the University of Massachusetts and the Infrared Processing and Analysis Center/California Institute of Technology, funded by the National Aeronautics and Space Administration and the National Science Foundation.

References

Acke, B. & van den Ancker, M. E. 2004, *A&A*, 426, 151

- Acke, B. & van den Ancker, M. E. 2006, *A&A*, 457, 171
- Acke, B., van den Ancker, M. E., & Dullemond, C. P. 2005, *A&A*, 436, 209
- Andrillat, Y. & Jaschek, C. 1998, *A&AS*, 131, 479
- Benedettini, M., Pezzuto, S., Giannini, T., Lorenzetti, D., & Nisini, B. 2001, *A&A*, 379, 557
- Berrilli, F., Lorenzetti, D., Saraceno, P., & Strafella, F. 1987, *MNRAS*, 228, 833
- Bouwman, J. 2001, PhD thesis, University of Amsterdam
- Bouwman, J., de Koter, A., van den Ancker, M. E., & Waters, L. B. F. M. 2000, *A&A*, 360, 213
- Damiani, F., Micela, G., & Sciortino, S. 2006, *A&A*, 447, 1041
- de Winter, D., van den Ancker, M. E., Maira, A., et al. 2001, *A&A*, 380, 609
- di Francesco, J., Evans, II, N. J., Harvey, P. M., Mundy, L. G., & Butner, H. M. 1994, *ApJ*, 432, 710
- Drew, J. E., Busfield, G., Hoare, M. G., et al. 1997, *MNRAS*, 286, 538
- Dullemond, C. P. 2002, *A&A*, 395, 853
- Dullemond, C. P., Dominik, C., & Natta, A. 2001, *ApJ*, 560, 957
- Eisner, J. A., Lane, B. F., Akeson, R. L., Hillenbrand, L. A., & Sargent, A. I. 2003, *ApJ*, 588, 360
- Ekström, S., Meynet, G., Maeder, A., & Barblan, F. 2008, *A&A*, 478, 467
- Han, F., Mao, R. Q., Lu, J., et al. 1998, *A&AS*, 127, 181
- Henning, T., Burkert, A., Launhardt, R., Leinert, C., & Stecklum, B. 1998, *A&A*, 336, 565
- Lagage, P. O., Pel, J. W., Authier, M., et al. 2004, *The Messenger*, 117, 12
- Leinert, C., Graser, U., Przygodda, F., et al. 2003, *Ap&SS*, 286, 73
- MacFadyen, A. I. & Woosley, S. E. 1999, *ApJ*, 524, 262
- Maeder, A. 1987, *A&A*, 178, 159
- Maeder, A. & Meynet, G. 2000, *ARA&A*, 38, 143
- Malbet, F., Benisty, M., de Wit, W.-J., et al. 2007, *A&A*, 464, 43
- Mannings, V. 1994, *MNRAS*, 271, 587
- Manoj, P., Ho, P. T. P., Ohashi, N., et al. 2007, *ApJ*, 667, L187
- Meynet, G. & Maeder, A. 2000, *A&A*, 361, 101
- Millan-Gabet, R., Schloerb, F. P., & Traub, W. A. 2001, *ApJ*, 546, 358
- Monnier, J. D., Berger, J.-P., Millan-Gabet, R., et al. 2006, *ApJ*, 647, 444
- Monnier, J. D., Millan-Gabet, R., Billmeier, R., et al. 2005, *ApJ*, 624, 832
- Oudmajer, R. D. & Drew, J. E. 1999, *MNRAS*, 305, 166
- Palla, F. & Prusti, T. 1993, *A&A*, 272, 249
- Petrov, R. G., Malbet, F., Weigelt, G., et al. 2007, *A&A*, 464, 1
- Porter, J. M. & Rivinius, T. 2003, *PASP*, 115, 1153
- Savage, B. D. & Mathis, J. S. 1979, *ARA&A*, 17, 73
- Shu, F., Najita, J., Ostriker, E., et al. 1994, *ApJ*, 429, 781
- Skinner, S. L., Brown, A., & Stewart, R. T. 1993, *ApJS*, 87, 217
- Steenman, H. & Thé, P. S. 1989, *Ap&SS*, 159, 189
- Steenman, H. & Thé, P. S. 1991, *Ap&SS*, 184, 9
- Tatulli, E., Millour, F., Chelli, A., et al. 2007, *A&A*, 464, 29
- Terada, H., Imanishi, M., Goto, M., & Maihara, T. 2001, *A&A*, 377, 994
- van Boekel, R. 2004, PhD thesis, University of Amsterdam
- Vink, J. S., Drew, J. E., Harries, T. J., & Oudmajer, R. D. 2002, *MNRAS*, 337, 356
- Vink, J. S., O'Neill, P. M., Els, S. G., & Drew, J. E. 2005, *A&A*, 438, L21
- Vinković, D., Ivezić, Ž., Jurkić, T., & Elitzur, M. 2006, *ApJ*, 636, 348
- Wolf, C. & Podsiadlowski, P. 2007, *MNRAS*, 375, 1049
- Woosley, S. E. & Heger, A. 2006, *ApJ*, 637, 914